Verification of DES for Flow over Rigidly and Elastically-Mounted Circular Cylinders in Normal and Yawed Flow

Xingeng Wu[1], Mohammad Jafari[1], Partha Sarkar[2], Anupam Sharma[3,*]

Department of Aerospace Engineering, Iowa State University, Ames, Iowa, 50011

Abstract

A computational approach based on a $k - \omega$ delayed detached eddy simulation model for predicting aerodynamic loads on a smooth circular cylinder is verified against experiments. Comparisons with experiments are performed for flow over a rigidly-mounted (static) cylinder and for an elastically-mounted rigid cylinder oscillating in the transverse direction due to vortex-induced vibration (VIV). For the static cases, measurement data from the literature is used to validate the predictions for normally-incident flow. New experiments are conducted as a part of this study for yawed flow, where the cylinder axis is inclined with respect to the inflow velocity at the desired yaw angle, $\beta = 30°$. Good agreement is observed between the predictions and measurements for mean and rms surface pressure. Three yawed flow cases ($\beta = 15°, 30°, \& 45°$) are simulated and the results are found to be independent of β (independence principle) when the flow speed normal to the cylinder axis is selected as the reference velocity scale.

Dynamic (VIV) simulations for an elastically-mounted rigid cylinder are performed by coupling the flow solver with a solid dynamics solver where the cylinder motion is modeled as a mass-spring-damper system. The simulations accurately predict the displacement amplitude and unsteady loading over a wide range of reduced velocity, including the region where "lock-in" occurs. VIV simulations are performed at two yaw angles, $\beta = 0°$ and $45°$ and the independence principle is found to be valid over the range of reduced velocities tested

---

*Corresponding author

Email address: `sharma@iastate.edu` (Anupam Sharma)

[1]PhD Student

[2]Professor, Iowa State University

[3]Associate Professor, Iowa State University

with a slightly higher discrepancy when the vortex shedding frequency is close to the natural frequency of the system.

1. Introduction

Inclined and horizontally- or vertically-spanned cylinder are used in various engineering applications: cable-stayed, suspension, and tied-arch bridges, power transmission lines, off-shore risers, sub-sea pipelines etc. These cylinders are prone to large-amplitude flow-induced vibration, which can lead to catastrophic failure of the cylinders and the structures supported by them. The vibration mechanisms involve complex aeroelastic (motion-induced) interactions that depend on the spatial orientation, geometry, surface-characteristics, and dynamic properties of the cylinders. Davenport (1995) shows that large amplitude vibrations can lead to either catastrophic- or fatigue failure of the cylinders and/or of the adjoining structures, which poses a significant threat to the safety and serviceability of these systems.

Flow induced vibration can be classified into the following categories: Kármán vortex-induced vibration (VIV), rain-wind induced vibration (RWIV), wake-induced vibration, and dry- or iced-cable galloping. While VIV and RWIV occur at relatively low wind speeds ($<$ 20 m/s), wake-induced vibration and dry-cable galloping occur at higher speeds. Simulation of any of these aeroelastic phenomena requires accurate computation of the aerodynamic loads acting on the cable. This paper presents a comprehensive verification of a high-fidelity flow simulation technique (detached eddy simulations or DES) for flow over rigidly and elastically-mounted rigid circular cylinders in normal and yawed flow. Yaw angle (β) is defined as the angle between the cylinder axis and a vector orthogonal to the flow velocity vector in the plane of the cylinder axis. Yawed flow is considered because RWIV and dry-cable galloping occur only when β is non-zero. The diameter-based Reynolds number (Re_D) in the simulations is 2×10^4. At this Re_D, the boundary layer is laminar when it separates and transitions to turbulence in the free shear layer. The results of this paper are presented in two parts - the first part deals with rigidly-mounted (static) cylinders and the second part addresses elastically-mounted cylinders.

In the first part of the paper, simulations of flow over a static cylinder are verified with measurements from the literature as well as new experiments that are performed for $\beta = 0°$ and $30°$ as a part of this study. Comparisons between the simulations and the measurements include mean and rms of surface pressure, mean wake velocity profile, and power spectra of lift and drag. The agreement with the measured data ranges from very good to acceptable. Simulations are performed for four values of β ($= 0°$, $15°$, $30°$, and $45°$) and the validity of the *independence principle* (IP) is examined. According to IP, the aerodynamic loads scaled using the velocity component normal to the cylinder axis are independent of β (Zdravkovich (2003)). Prior research (see e.g., Franzini et al. (2009) and Zhao et al. (2009)) has suggested the validity of IP for β up to $45°$. The results of yawed flow simulations confirm the validity of IP for the static configurations analyzed.

The second part of the paper deals with vortex-induced vibrations (VIV). VIV are self-excited oscillations caused by the unsteady lift generated on a cylinder as a result of the vortex shedding in its wake. VIV is a common occurrence in many engineering structures, e.g., transmission lines, stacks, bridges, and offshore platform supports. Of particular interest is the phenomenon of "lock-in" or "synchronization" which occurs when the vortex-shedding frequency gets locked in with the natural frequency of the system. High but finite-amplitude (limit-cycle) oscillations are observed in this resonance condition due to non-linearity in the system. These high-amplitude oscillations can cause significant damage to the structure. VIV has been investigated extensively in the past few decades due to its practical significance. Bearman (1984), Sarpkaya (2004) and Williamson and Govardhan (2004) present detailed reviews of the research on this topic.

Investigations of VIV over the past several decades, have resulted in an improved understanding of the phenomenon. Until recently, most of these investigations considered relatively high mass-damping systems. In the last two decades, VIV of low mass-damping systems has garnered considerable interest due to the applicability of the phenomenon in marine engineering and offshore wind turbines (mooring lines). Such low mass-damping systems have been largely investigated using experiments (e.g., Jain and Modarres-Sadeghi (2013) and Franzini et al. (2013)) and semi-analytical methods that model vortex shedding using the classical Van der Pol oscillator (e.g., Xu et al. (2008)).

Experiments of VIV in low mass-damping systems have been typically conducted in water channels with partially or fully-submerged cylinders. Such setup can suffer from finite-span effects due to different end conditions on the two ends – wall on one side and free surface on the other. These effects are distinctly observable in yawed flow measurements (see e.g., Franzini et al. (2013)) where the results are found to be dependent on the direction with respect to the flow the cylinder is yawed (i.e., $\beta = 45°$ versus $-45°$). Computer simulations do not suffer from end effects as periodic boundary conditions enable modeling an infinitely long cylinder, although periodicity can introduce artificial effects if spanwise coherence length is greater than the simulated span.

Numerical computations of VIV of low mass-damping systems have been performed using the Reynolds Averaged Navier-Stokes (RANS) equations (e.g., Guilmineau and Queutey (2004)), large eddy simulations or LES (e.g., Al-Jamal and Dalton (2004)), and direct numerical simulations or DNS (e.g., Lucor et al. (2005), Evangelinos et al. (2000), and Dong and Karniadakis (2005)). While the DNS approach is attractive from the perspective of resolving the entire turbulence spectrum, it is only feasible for very low Re_D flows due to the associated computation cost. Large Eddy Simulation (LES) is more feasible at moderate Re_D while Detached Eddy Simulations (DES) can be used over a very large range of Re_D without making the computations prohibitively expensive. The DES approach is used here.

The phenomenon of VIV is investigated with elastically-mounted cylinder simulations and the results are verified against measured data available in the literature. The VIV simulations are also performed at multiple values of β ($= 0°$ and $45°$) to investigate the validity of the independence principle for VIV of low mass-damping systems. With the detailed comparisons against measurements for rigidly-mounted and elastically-mounted oscillating cylinder presented here, this paper serves as a benchmark for the accuracy of the DES technique in predicting aerodynamic loads on stationary cylinders and cylinders in dynamic motion.

2. Computational Methodology

The flow is approximated to be incompressible since the flow Mach number is less than 0.2. Various degrees of approximations can be utilized to model flow turbulence: from resolving only time-averaged quantities in Reynolds Averaged Navier-Stokes or RANS, to

resolving the tiniest of turbulent eddies in Direct Numerical Simulations or DNS. Large eddy simulations (LES) resolve energy containing eddies but model the net effect of smaller (unresolved/universal) eddies on larger (resolved) eddies. The detached eddy simulation (DES) technique (Spalart et al., 1997) is a hybrid approach that uses RANS equations to simulate attached flow near solid surfaces and LES for separated (detached) flow away from the surfaces. DES allows computation of high Reynolds number flows relatively inexpensively by removing the constraint in LES to have very fine grids near solid boundaries.

Flow over stationary slender structures with circular cross-section has been studied using unsteady RANS (Pontaza et al., 2009), DES (Travin et al., 2000; Yeo and Jones, 2011, 2012), LES (Breuer, 1998; Kravchenko and Moin, 2000; Catalano et al., 2003), and DNS (Dong and Karniadakis, 2005; Zhao et al., 2009) approaches. Detailed flow simulations have been performed using DES for a single, stationary, yawed cylinder in uniform inflow (Yeo et al., 2007; Yeo and Jones, 2008) and oscillating inflow (Yeo and Jones, 2012). DES has also been used to investigate the use of strakes in cables for aerodynamic mitigation of wind-induced oscillations by Yeo and Jones (2011). In essence, high-fidelity simulations have been instrumental in gaining insights into the problem of flow-induced vibration.

In LES and DES, the equations are spatially filtered (low-pass) and the numerical procedure solves for the filtered quantities that can be resolved by the grid. The sub-filter (or sub-grid) quantities exert a "stress" on the filtered flow-field, which is modeled using a sub-grid scale (SGS) stress model. Denoting spatially filtered quantities by overhead tilde ($\tilde{\ }$), the incompressible flow equations with an eddy-viscosity turbulence model are

$$\frac{\partial \tilde{U}_i}{\partial x_i} = 0, \text{ and}$$

$$\frac{\partial \tilde{U}_i}{\partial t} + \frac{\partial (\tilde{U}_j \tilde{U}_i)}{\partial x_j} = -\frac{1}{\rho}\frac{\partial \tilde{p}}{\partial x_i} + \nu \frac{\partial^2 \tilde{U}_i}{\partial x_j^2} - \frac{\partial \tau_{ij}}{\partial x_j}, \tag{1}$$

where $\tau_{ij} = \widetilde{U_i U_j} - \tilde{U}_i \tilde{U}_j = -2\,\nu_{SGS}\,\tilde{S}$ and $\tilde{S} = (\partial \tilde{U}_i/\partial x_j + \partial \tilde{U}_j/\partial x_i)/2$. In the above, SGS denotes a sub-grid scale quantity, τ_{ij}^{SGS} denotes the sub-grid scale stress tensor which is modeled as the product of the eddy viscosity, ν_{SGS} and the strain rate tensor S_{ij}; turbulence models of such type are referred to as eddy-viscosity models. DES is a non-zonal hybrid RANS-LES method, where a RANS turbulence model is used to compute the eddy viscosity for the SGS stress tensor in the corresponding LES. In the original DES formulation (Spalart

5

et al. (1997)), the Spalart-Allmaras (SA) LES and SA-RANS models were used. We use the method developed by Yin et al. (2015), which introduces a dynamic procedure to improve the DES capability by correcting for modeled stress depletion and log-layer mismatch. This model has been implemented in the open source CFD software OpenFOAM. All the simulations results in this paper are obtained using OpenFOAM. The numerical scheme uses second order backward difference for time integration and linear interpolation with central differencing for spatial discretization of the governing equations.

2.1. Detached Eddy Simulation Model

A summary of the DES model used in this study is provided here; details are available in Yin et al. (2015). It uses a $k - \omega$ turbulence closure model in the RANS zones, and the same model is used to calculate ν_T in the LES zones. The eddy viscosity in the $k - \omega$ DDES can be defined as $\nu_T = l_{DDES}^2 \omega$, where l_{DDES} is the DDES length scale. The different length scales in the $k - \omega$ DDES model are defined as

$$
\begin{aligned}
l_{DDES} &= l_{RANS} - f_d \max(0, \ l_{RANS} - l_{LES}), \\
l_{RANS} &= \sqrt{k}/\omega, \\
l_{LES} &= C_{DES} \triangle .
\end{aligned}
\tag{2}
$$

In the above, l_{RANS} and l_{LES} are the length scales of the RANS and LES branches respectively and $\triangle = f_d V^{1/3} + (1 - f_d) h_{max}$, where $h_{max} = \max(dx, dy, dz)$ is the maximum grid size, and f_d is a shielding function of the DDES model, defined as $f_d = 1 - \tanh\{(8\,r_d)^3\}$, with

$$
r_d = \frac{k/\omega + \nu}{\kappa^2 \, d_w^2 \, \sqrt{U_{i,j} U_{i,j}}},
$$

ν is the molecular viscosity, κ is the von Kármán constant, d_w is the distance between the cell and the nearest wall, and $U_{i,j} = \partial_j U_i$ is the velocity gradient. In the RANS branch, the transport equation for k and ω are written as

$$
\begin{aligned}
\frac{Dk}{Dt} &= 2\nu_T |S|^2 - C_\mu k\omega + \partial_j[(\nu + \sigma_k \nu_T)\partial_j k], \\
\frac{D\omega}{Dt} &= 2C_{\omega 1} |S|^2 - C_{\omega 2}\omega^2 + \partial_j[(\nu + \sigma_\omega \nu_T)\partial_j \omega],
\end{aligned}
\tag{3}
$$

$$
\text{where } \nu_{\mathrm{T}} = \mathrm{k}^2/\omega.
$$

In the LES region ($f_d = 1, l_{DDES} = C_{DES} \triangle$), the eddy viscosity switches to $\nu_T = l^2_{DDES} \omega = (C_{DES}\triangle)^2 \omega$, which is similar to the eddy viscosity in the Smagorinsky model, $\nu_s = (C_s \triangle)^2 |S|$.

The LES branch of this $k - \omega$ DDES model uses a dynamic procedure which defines the value of C_{DES} as

$$
\begin{aligned}
C_{DES} &= \max(C_{lm}, \ C_{dyn}), \\
C^2_{dyn} &= \max\left(0, \ 0.5\frac{L_{i,j}M_{i,j}}{M_{i,j}M_{i,j}}\right), \\
C_{lim} &= C^0_{DES}\left[1 - \tanh\left(\alpha\exp\left(\frac{-\beta\,h_{max}}{L_k}\right)\right)\right], \\
C^0_{DES} &= 0.12, \quad L_k = \left(\frac{\nu^3}{\epsilon}\right)^{\frac{1}{4}}, \quad \alpha = 25, \quad \beta = 0.05, \\
\epsilon &= 2\left(C^0_{DES}h_{max}\right)^2 \omega\,|S|^2 + C_\mu k\,\omega.
\end{aligned}
\tag{4}
$$

For further details about the DES model, the reader is referred to Yin et al. (2015).

2.2. Solid Body Dynamics and Coupling

Simulations of VIV are performed with the pimpleDyMFoam solver which uses the *sixD-oFRigidBodyMotion* feature of OpenFOAM. For each timestep, pimpleDyMFoam solver calculates the motion and updates the displacement of the cylinder by integrating the following equation in time using the Crank-Nicolson method.

$$
m\ddot{y} + c\dot{y} + ky = F_{fluid},
\tag{5}
$$

where m is the mass of the rigid cylinder, $\ddot{y}$, $\dot{y}$, and y are the instantaneous acceleration, velocity and displacement of the cylinder, respectively, c is the damping of the system, k is the spring stiffness and F_{fluid} is the transverse (cross-stream) component of the fluid force acting on the cylinder surface.

In order to maintain the quality of the meshes inside the boundary layer in dynamic simulations, the mesh around the cylinder (up to 1 diameter from the cylinder axis) moves with the cylinder without deforming. The mesh away from the cylinder is deformed based on the position of the cylinder. The solver then updates the fluxes according to the motion and uses the PIMPLE method to solve the incompressible Navier-Stokes equations.

7

2.3. Computational Grid and Mesh Sensitivity Study

The outer boundary of the computational domain is circular with a radius of $25 \times D$, where D is the diameter of the cylinder. The cylinder is placed in the center of the domain and the span dimension is $10 \times D$ for all the simulations presented here. Periodic boundary conditions are used in the span direction, while freestream condition is used on the outer radial boundary. The domain is discretized using a multi-block grid that has three blocks: (1) an O-grid is used to resolve the flow around the cylinder, (2) an H-grid to resolve the wake, and (3) a C-grid for the far field. In order to accurately capture the aerodynamic forces on the cylinder, the flow around the cylinder and in the near-wake region has to be resolved with high precision. A fine mesh is therefore applied in these regions. Figure 1 shows a cross-sectional view of the full computational domain as well as a zoom-view to highlight the grid topology.

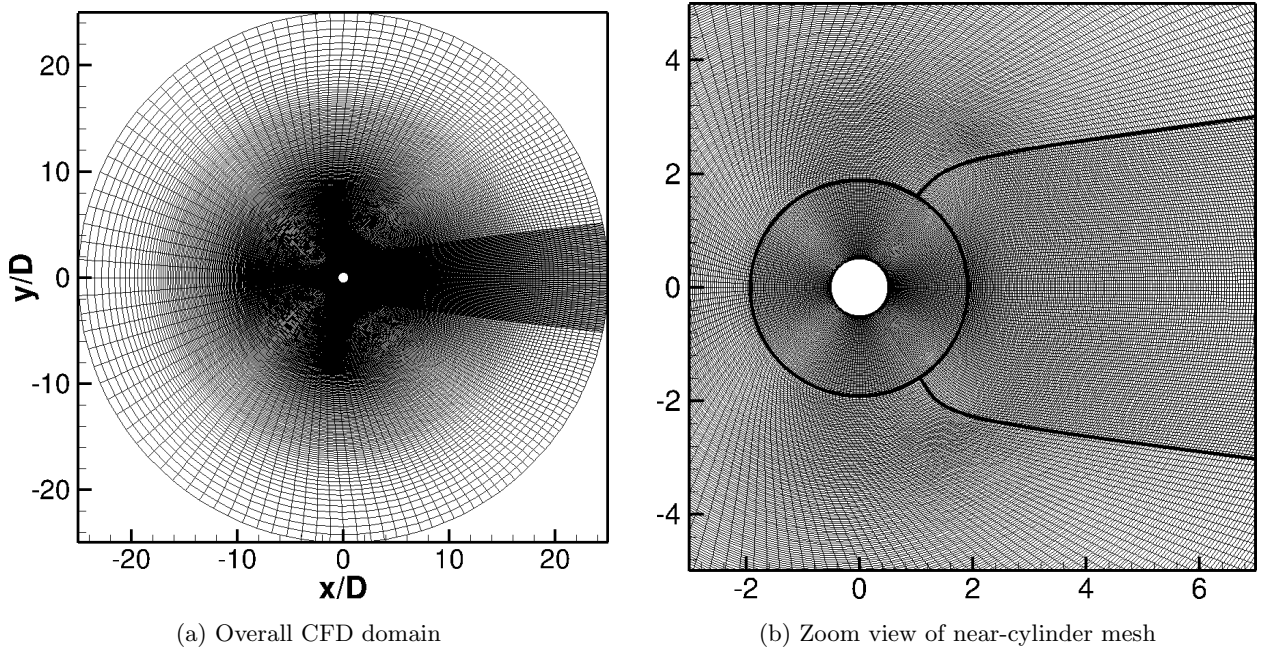(a) Overall CFD domain

(b) Zoom view of near-cylinder mesh

Figure 1: Cross-sectional views of the computational grid

A mesh sensitivity study is performed for normally-incident flow. Table 1 provides a summary of the different cases simulated for this study. Three different meshes, labeled 'Mesh 1', 'Mesh 2', and 'Mesh 3' are shown in the table. The computational domain is $25 \times D$ in the radial direction and $10 \times D$ in the span direction.

8

Table 1: Summary of the test cases simulated to investigate sensitivity of results to mesh size add average y^+ values and some results here like back pressure, rms C_p, etc. same as in Table 2

Mesh name	Cell counts (θ, r, z)
Mesh 1	157, 233, 65
Mesh 2	236, 343, 100
Mesh 3	354, 507, 150

Figure 2 compares the mean aerodynamic pressure coefficient, $\overline{C}_p = 2(\bar{p} - p_\infty)/(\rho V_\infty^2)$ obtained using the simulations with the different grids, and the experimental data. Experiment I refers to the data from Norberg (2013) and Exp-ISU is from our measurements (Section 3 provides the details). Simulations are performed at $Re_D = 20,000$, which is the same as Experiment I, but the Re_D in Exp-ISU is higher ($= 51,500$) due to the limitation of the wind tunnel and the measurement equipment.

Consistent with the results of Travin et al. (2000) and Breuer (2000), the simulation results are found to be sensitive to mesh size even with the highest mesh resolution attempted. Mesh 2 and Mesh 3 capture the flow separation location correctly (same as in the experiment), but separation is delayed with Mesh 1. Results of Mesh 2 are in close agreement with Experiment I, however they differ from the results of Mesh 3 in the separated flow region. Interestingly, the Exp-ISU data agrees well with Mesh 3 results in the same region. Based on this study, Mesh 2 is chosen for the subsequent simulations because it can predict aerodynamic loading and resolve wake turbulence reasonably accurately, and has a modest computational cost.

3. Experimental Setup and Measurements

Static wind tunnel experiments were conducted on a smooth cylinder of circular cross section representing a stay cable to measure the aerodynamic forces and the velocity distribution in its wake. These experiments were performed in the Aerodynamic/Atmospheric Boundary Layer (AABL) Wind and Gust Tunnel located in the Department of Aerospace
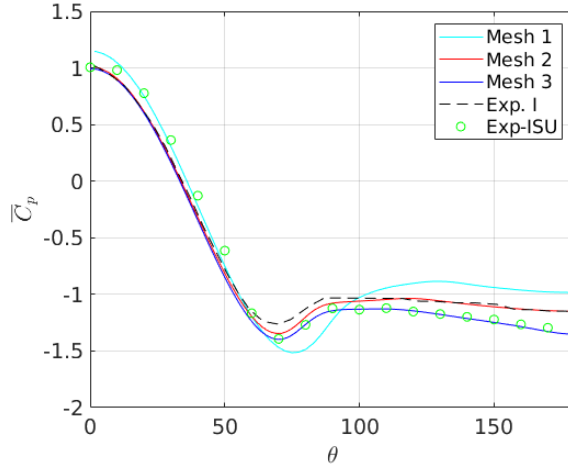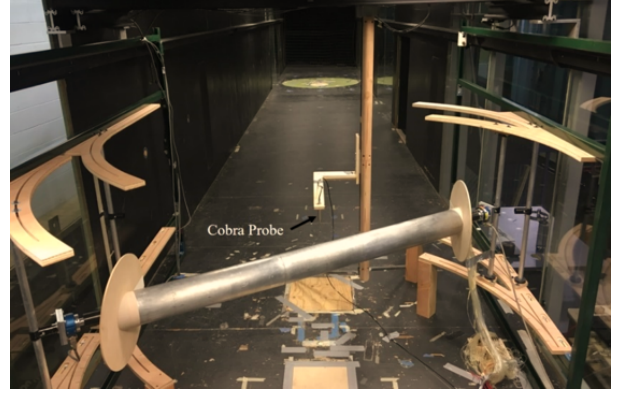
Figure 2: $\overline{C}_p$ comparisons between simulation results using different meshes.

Engineering at Iowa State University. This wind tunnel has an aerodynamic test section of 2.44 m (8.0 ft) width × 1.83 m (6.0 ft) height and a design maximum wind speed of 53 m/s (173.9 ft/s). A polished aluminum tube with diameter, $D = 0.127$ m and length, $L = 1.52$ m was selected as the smooth cylinder model. Although the aspect ratio ($L/D = 12$) is sufficiently large to minimize edge effects at the mid-span of the circular cylinder, two circular plates of diameter $4D$ were attached to the ends of the cylinder. These plates were adjusted for each cylinder yaw angle to be parallel to the incoming airflow so that nearly 2D flow could be achieved over the cylinder. The blockage ratio in the tunnel with the model was approximately 5% for all measurements. Figure 3 displays the model setup in the AABL tunnel with the cylinder in normal-flow and yawed-flow configurations. An innovative multi-functional static setup was designed to measure the pressure distributions and velocity profiles for different yaw angles. As shown in Fig. 3, this setup properly secures the model for different yaw angles.

The model has 128 pressure taps distributed on its surface to measure local instantaneous pressure (see Fig. 4). These pressure values are used to compute aerodynamic lift and drag (viscous part ignored) on the cylinder as well as pressure correlations along the span. There are 36 pressure taps at equal angular spacing of 10 degrees along each of the three rings located on the cylinder. The three rings are labeled Right (R), Middle (M), and Left (L) as seen in Fig. 4 (a) and are spaced $4D$ and $5D$ apart from each other along the span. Another
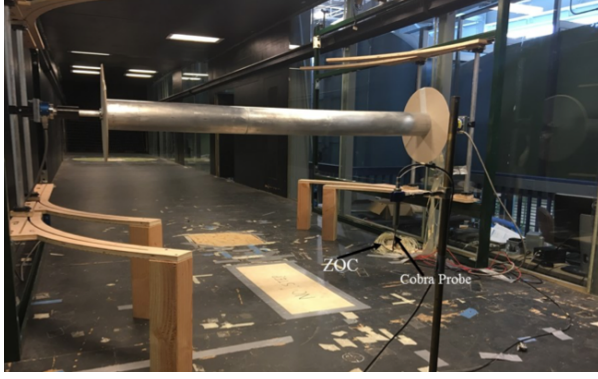
(a) setup for normal-flow measurements   (b) setup for yawed flow measurements

Figure 3: Pictures showing the model setup used to allow measurements at arbitrary inflow angles. The Cobra probe used to measure the wake is shown in (a).

set of pressure taps are located at a fixed angular location at equal spacing of $1D$ along the span between the rings (see Fig. 4 (a,b)).

3.1. Data Acquisition System

For wake measurement, one Cobra Probe (4-hole velocity probe) mounted on a traverse system was used to measure the velocity field behind the model (see Fig. 3 (a)). In order to minimize the blockage effect of the traverse system, its cross section was streamlined by using an airfoil section. For velocity measurements, the sampling rate was 1250 Hz and the sampling time was 60 s. Wake measurements were made $2.5D$ downstream of the model (measured from the cylinder axis), where the turbulence intensity was lower than the maximum allowable value (overall 30%) for the Cobra Probe.

Two 64-channel pressure modules (Scanivalve ZOC 33/64 Px) were utilized to capture the local pressure. In addition, an Ethernet remote A/D system (ERAD) was used as a collection system to read information from the ZOC. The sampling rate and sampling time for all pressure measurements were 250 Hz and 60 s respectively. The Scantel program from Scanivalve was used for pressure data acquisition. In order to minimize the error of measurement due to the tube length, both ZOCs were placed inside the wind tunnel near the model (Fig. 3 (b)). The wake measurement traverse system was removed when surface pressure measurements were made.

11

(a) Pressure taps on the cylinder model

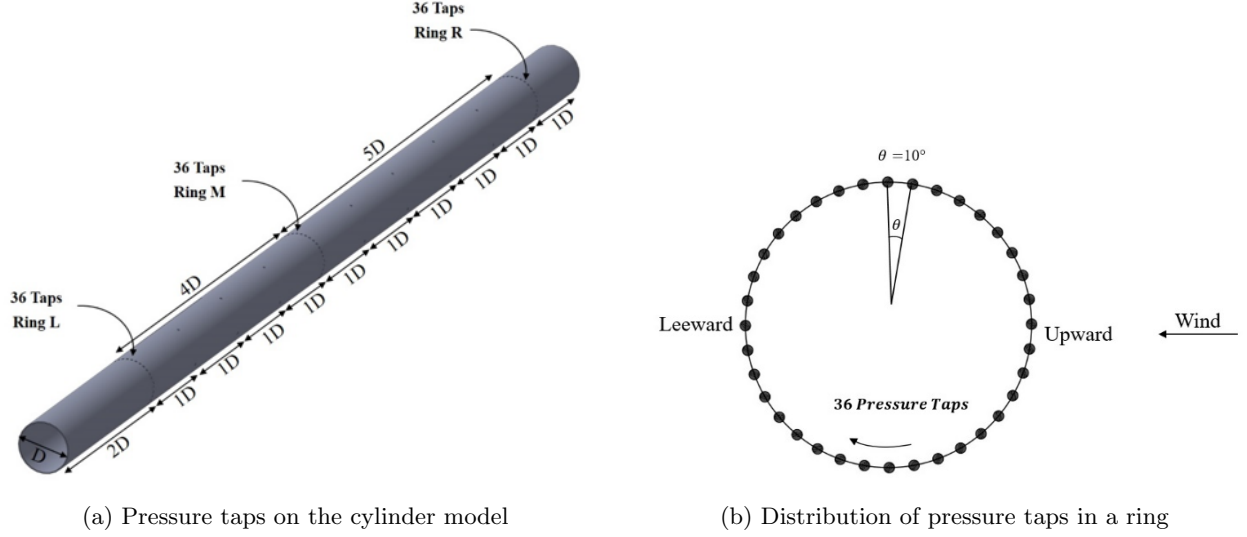(b) Distribution of pressure taps in a ring

Figure 4: Schematics illustrating the locations of surface pressure taps on the cylinder model.

4. Static-Cylinder Results

The objective of this paper is to demonstrate the capability of DES to predict aerodynamic loads on a static cylinder and an elastically-mounted cylinder. This section discusses the results of the simulations of flow over a static cylinder.

Simulations are performed for (1) flow normal to the cylinder axis, and (2) flow at an angle to the cylinder axis (inclined/yawed cylinder); three yaw angles (β) are analyzed in this study. Smooth inflow is used – zero turbulence in the numerical simulations and the minimum possible inflow turbulence intensity ($\sim$0.2%) in the tunnel. Cylinder surface is very smooth and hence surface roughness is not modeled in the simulations. Verification is performed with existing experimental data in the literature, as well as data from new experiments conducted as a part of this study.

4.1. Normally-Incident Flow

Table 2 summarizes the simulation results for the static cases and compares them with two sets of experimental data. The peak shedding Strouhal number (St_p), the mean drag coefficient, $\overline{C}_d$ and the mean back pressure coefficient, $\overline{C}_{pb}$ are compared in the table. Strouhal number is a non-dimensional frequency, defined as $St = f\,D/V_\infty$, and St_p corresponds to the peak vortex shedding frequency of the cylinder.
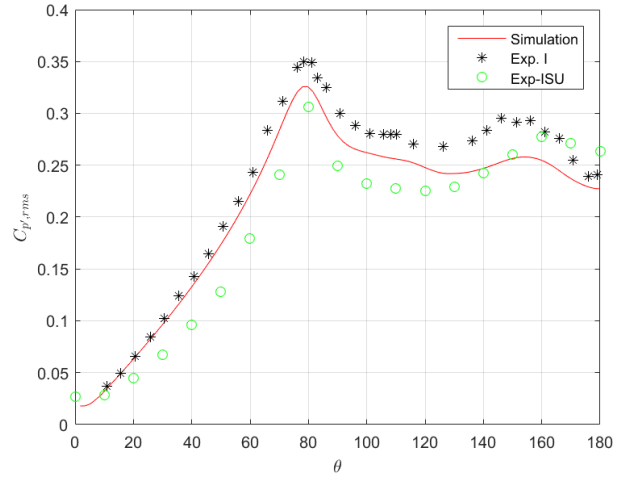
Figure 5 compares the predicted mean aerodynamic pressure coefficient, $\overline{C}_p$ and the root mean square of perturbation pressure coefficient, $C_{p'rms} = \left(\overline{C_p^2 - \overline{C}_p^2} \right)^{1/2}$ with the data from the two experiments. The predicted $\overline{C}_p$ agrees very well with the data from Experiment I; Exp-ISU data shows slightly lower $\overline{C}_p$ than observed in Experiment I and the simulation, especially after 100°, and the mean back pressure, $\overline{C}_{pb}$ is lower as well. The predicted $C_{p'rms}$ distribution lies in between the two measurements. Both measurements as well as the simulation show the peak to be around 80°, which indicates the location of flow separation. The predicted distribution over the cylinder surface agrees well with the measurements.

Table 2: Summary of results for normally-incident flow simulations

Re_D	Method	St_p	$\overline{C}_d$	$\overline{C}_{pb}$
20,000	$k - \omega$ DDES	0.21	1.13	-1.16
20,000	Experiment I	0.19	1.22	-1.1
51,500	Exp-ISU	0.21	1.14	-1.3
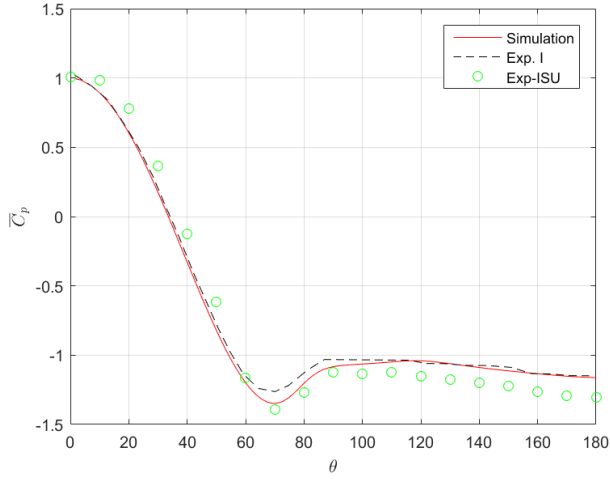
(a) Mean aerodynamic pressure coeff., $\overline{C}_p$

(b) r.m.s. of pressure coeff., $C_{p'rms}$

Figure 5: Comparisons of mean and rms of aerodynamic pressure coefficient between the simulation and experimental measurements.

Figure 6 plots the predicted and measured wake velocity profiles at the axial station, $x/D = 2$; the cylinder axis is located at $x/D = 0$. The peak wake deficit and the wake

profile are predicted accurately. The measured data shows a slight asymmetry in the data, which is perhaps due to an asymmetry in the experimental setup (the distance from the tunnel wall between the top and bottom surfaces of the cylinder is slightly different). The simulation data is averaged over 120 wake shedding cycles and the experimental data is averaged over 540 cycles.
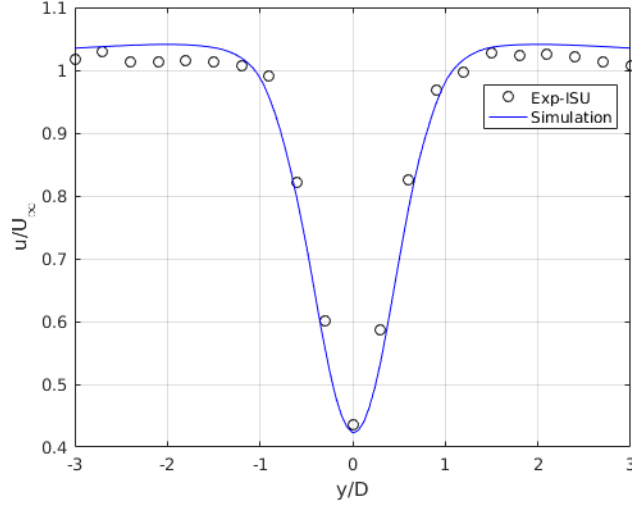

Figure 6: Comparison of predicted and measured velocity profiles in the cylinder wake $2D$ downstream of the cylinder axis.

Figure 7 presents predicted temporal variation of sectional lift and drag coefficients (C_l and C_d). As expected for a circular cylinder, the mean lift coefficient ($\overline{C}_l$) is zero but the mean drag coefficient ($\overline{C}_d$) is finite. The high-frequency oscillations, more apparent in C_l time history are due to Kármán vortex shedding, which occurs at $St = fD/U \sim 0.2$ for bluff bodies in the range of Re_D considered here. In addition to the oscillations at the Kármán vortex shedding frequency, the entire signal appears to modulate at a frequency which is an order of magnitude lower than that corresponding to $St = 0.2$. This modulation has a certain randomness to it and is not perfectly periodic. This modulation phenomenon has been reported elsewhere, see e.g., Travin et al. (2000).

Figure 8 (a) compares the power spectral densities of C_l between data from Exp-ISU and the simulation. The lift in the measurements is obtained by integrating the surface pressure measured using the pressure taps. Figure 8 (b) presents the DES computed spectra of C_d. Because vortex shedding alternates between the top and bottom sides of the cylinder, one
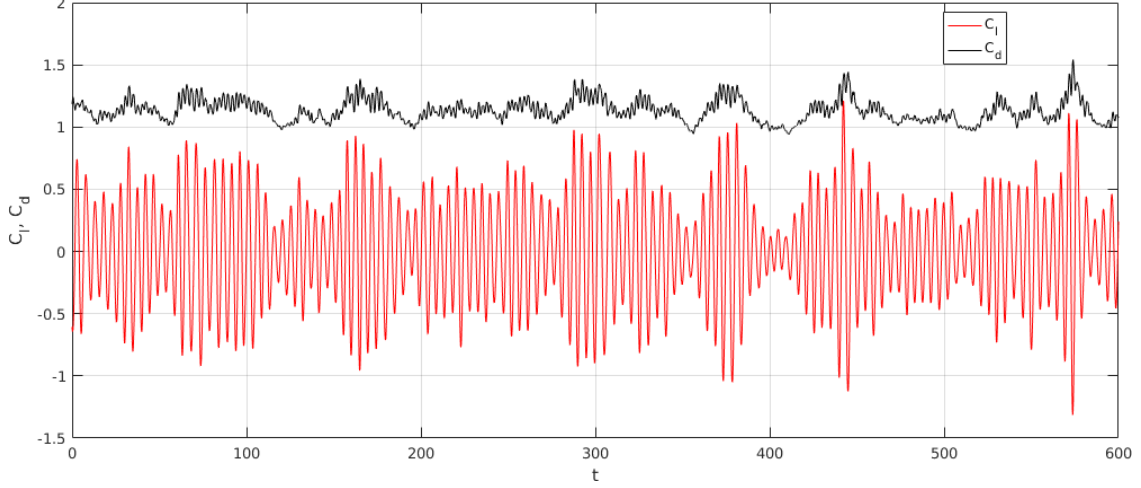
14

Figure 7: Predicted temporal variations of lift and drag coefficients

vortex shedding period contains two cycles of drag but only one cycle of lift. This can be seen in Figure 8, where the spectral peak for C_l occurs at f_p while the spectral peak for drag is at $2 \times f_p$, where f_p is determined by the peak shedding Strouhal number, $St_p = f_p D / V_\infty$. Based on existing literature (see Travin et al. (2000) and Norberg (2013)), $St_p \sim 0.2$. Both measurement and prediction agree very well with each other and show the peak for lift to be around f_p corresponding to St_p.
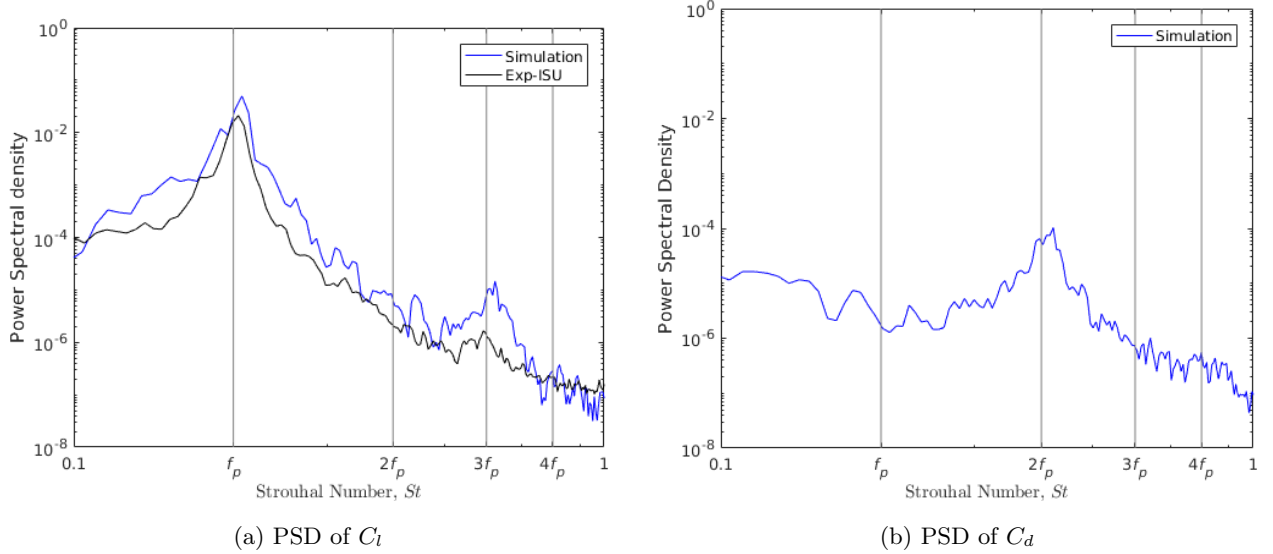

(a) PSD of C_l

(b) PSD of C_d

Figure 8: Comparison of predicted and measured power spectral densities (PSDs) of C_l and C_d. The measured data here is from our experiments (Exp-ISU).

The peak frequency and its first three harmonics that occur at $St = 0.4, 0.6, \& \, 0.8$, are

identified in the figure using vertical grid lines and labeled as $2f_p$, $3f_p$, & $4f_p$. The prediction and experiment both show a second, smaller peak in the lift spectrum at the third harmonic ($St = 0.6$). Since the lift vector alternates with the side the vortex sheds from, only odd harmonics of f_p (i.e., $3f_p$, $5f_p$, ...) are expected in the spectra. Therefore, no peak is observed in the lift spectra at the second harmonic ($St = 0.4$) or higher *even* harmonics in either the measured or the simulated data. The spectral shape of the PSD of C_l is correctly predicted, even though the magnitude is slightly higher than the measured data.

4.2. Yawed Flow (Inclined Cylinder)

The schematic in Fig. 9 illustrates the setup for the inclined-cylinder simulations. The relative inclination of the cylinder axis with respect to the flow is obtained by yawing the flow rather than inclining the cylinder; these simulations are therefore also referred to as yawed-flow simulations. Other than yawing the inflow, the setup is exactly the same as for normally-incident flow.

Yaw angle, β is defined as the angle between the inflow velocity vector $\boldsymbol{V_\infty}$ and the x axis; the cylinder is aligned with the z axis (see Fig. 9. The normal component of the flow velocity is $V_n = V_\infty \cos \beta$ and the spanwise component is $V_z = V_\infty \sin \beta$, where $V_\infty = |\boldsymbol{V_\infty}|$. The computational domain is $10 \times D$ in the spanwise direction to resolve and investigate spanwise variation of aerodynamic forces.

Table 3 summarizes the peak Strouhal number (St_p) and the back pressure coefficient (C_{pb}) for four different flow yaw angles, $\beta = 0, 15, 30$, & 45 degrees. The velocity component normal to the cylinder axis (V_n) is used as the reference velocity scale to define a new set of non-dimensional quantities, such as Reynolds number, $Re_{D,n} = \rho V_n D / \mu$, Strouhal number, $St_{p,n} = f\, D/V_n$, and aerodynamic pressure coefficient, $\overline{C}_{p,n} = 2(\bar{p} - p_\infty)/(\rho V_n^2)$. The peak shedding Strouhal number and the mean back pressure coefficient normalized in this manner are labeled respectively as $St_{p,n}$ and $\overline{C}_{pb,n}$. The measured value of $\overline{C}_{pb,n}$ is lower than that predicted by the simulations (see Table 3).

Figure 10 compares with measured data the predicted mean aerodynamic pressure coefficient ($\overline{C}_{p,n}$) and root mean square of perturbation pressure coefficient, $C_{p'rms,n}$ for $\beta = 30°$. The predicted back pressure ($\overline{C}_{pb,n}$) is found to be slightly higher than Exp-ISU data, which
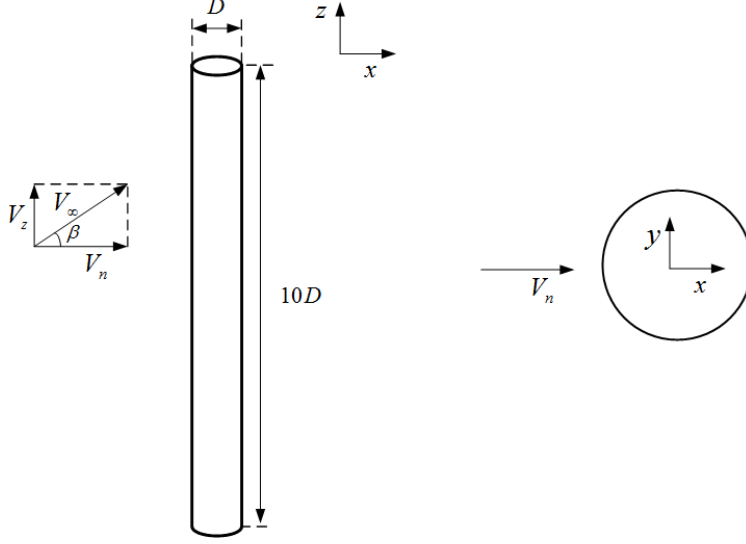
Figure 9: A schematic of the computational setup for static inclined cylinder simulations. The right figure is a cross-sectional view. The inflow is set to an angle with respect to the cylinder axis, which stays aligned with the z axis of the coordinate system.

Table 3: Summary of simulation results for four different flow yaw angles ($\beta = 0, 15, 30,$ & 45 deg). Experimental data is only shown for $\beta = 30°$.

Method	flow angle, β	Re_D	$Re_{D,n}$	$St_{p,n}$	$\overline{C}_{pb,n}$
Simulation	0°	20,000	20,000	0.21	-1.15
Simulation	15°	20,000	19,318	0.21	-1.11
Simulation	30°	20,000	17,320	0.20	-1.11
Exp-ISU	30°	51,500	44,600	0.19	-1.27
Simulation	45°	20,000	14,142	0.21	-1.16

is consisted with the observation for the normally-incident flow cases. The predicted $C_{p'rms,n}$ distribution agrees very well with measurement, especially for $\theta > 120°$, where θ is the angular position on the cylinder surface measured from upstream. The peak of $C_{p'rms,n}$ is observed around 80° in both experiment and simulation, which is indicative of the location of separation of the shear layer. For $\theta > 120°$, the measured data shows higher $C_{p'rms,n}$ than predicted by the simulations. A similar underprediction is observed in the normally-incident
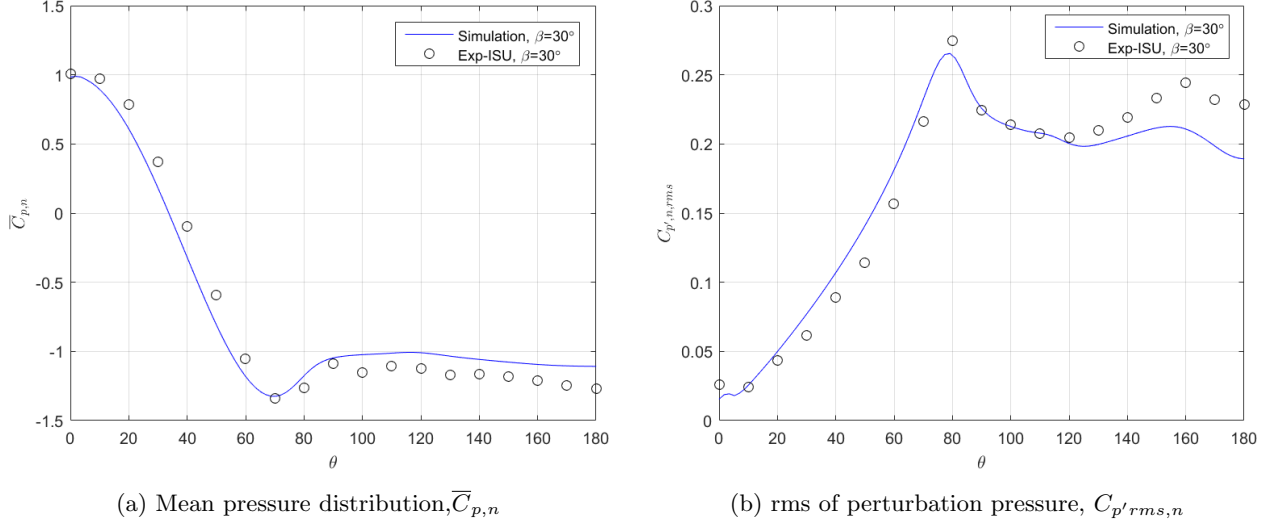
flow case.

(a) Mean pressure distribution, $\overline{C}_{p,n}$

(b) rms of perturbation pressure, $C_{p'rms,n}$

Figure 10: Comparisons between simulation and experimental measurements for $\beta = 30°$ yawed-flow case.

Figure 11 compares the predicted mean aerodynamic pressure coefficient ($\overline{C}_{p,n}$), for four different values of inflow yaw angle, β. The distribution of $\overline{C}_{p,n}$ is found to be very similar irrespective of β; Zdravkovich (2003) refers to this as 'independence principle' (IP). IP is also observed in the power spectral densities of the transverse force coefficient, $C_{y,n}$ for the same set of values of β analyzed. $C_{y,n} = 2\,f_y/(\rho V_n^2)$, where f_y is force per unit area in the y direction, and $C_{x,n}$ is correspondingly defined for the $x-$component of force. Figure 11 (b) shows that the spectra collapse when V_n is used to normalize the force coefficients and the frequency; the abscissa in Fig. 11 (b) is St_n.

Figure 12 shows spatio-temporal plots of the the force coefficients $C_{x,n}$ and $C_{y,n}$. The contours clearly show that $C_{x,n}$ and $C_{y,n}$ vary along the span, indicating that vortex shedding does not occur simultaneously along the entire span. In fact, a spatial drift from left to right with increasing time can be seen in the contours (more visible in the $C_{x,n}$ spatio-temporal plot) which is indicative of spanwise flow over the cylinder.

Figure 13 presents coherence of force coefficients for $\beta = 30°$ case. Magnitude squared coherence, $\gamma^2(\Delta z)$ is defined as

$$\gamma^2(\Delta z) = \frac{\langle|S_{xy}|^2\rangle}{\langle S_{xx}\rangle\langle S_{yy}\rangle}, \tag{6}$$

18

(a) Mean pressure coeff., $\overline{C}_{p,n}$
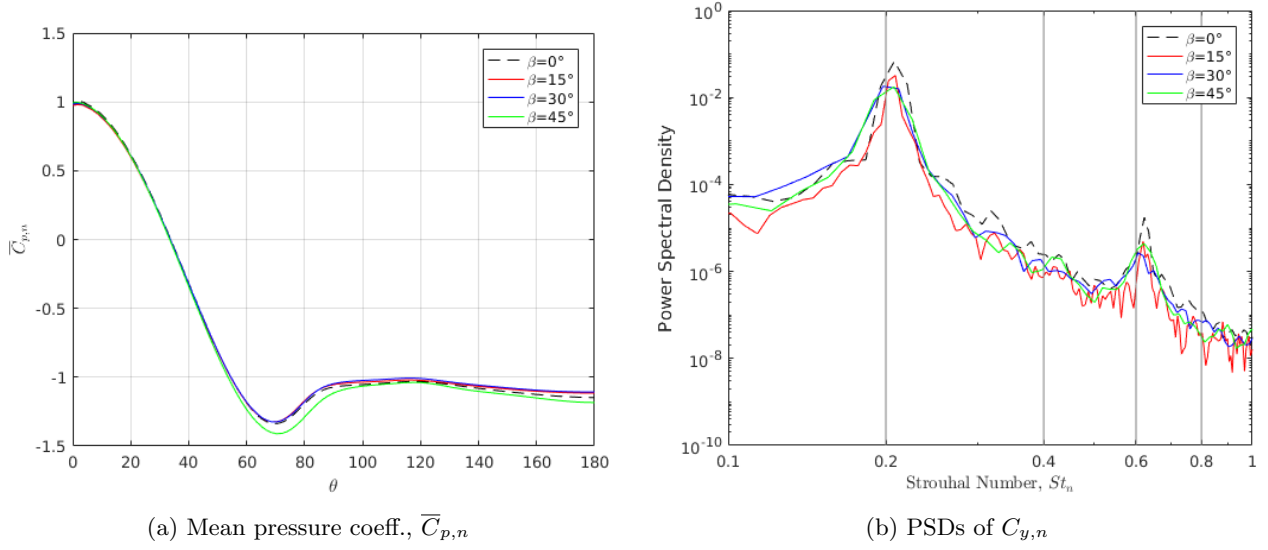
(b) PSDs of $C_{y,n}$

Figure 11: Independence principle: comparisons of (a) $\overline{C}_{p,n}$, and (b) power spectral densities (PSDs) of $C_{y,n}$ between predictions for various β values.
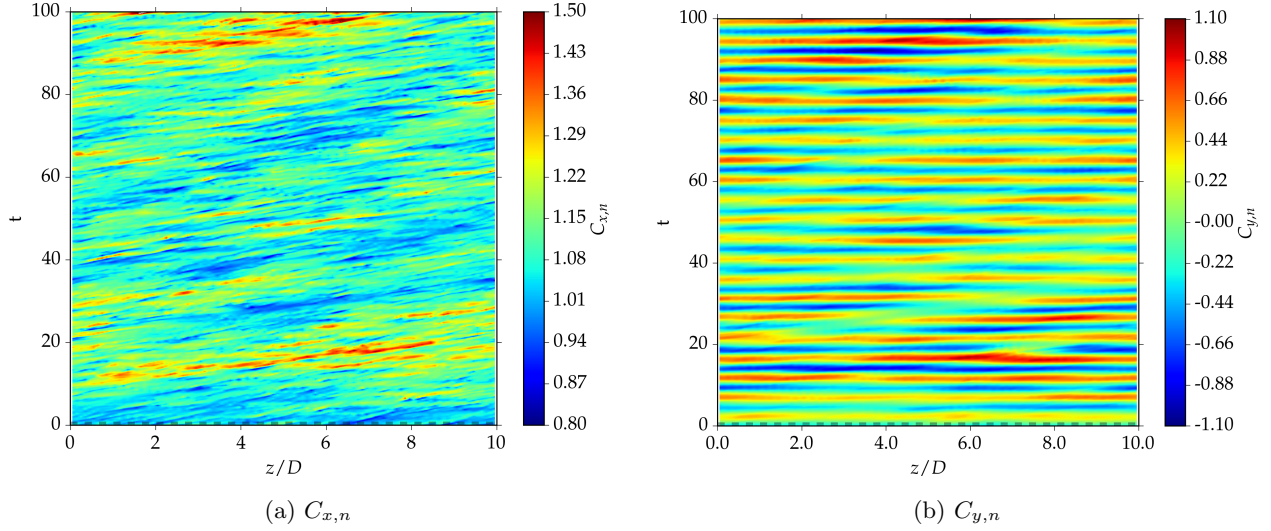

(a) $C_{x,n}$

(b) $C_{y,n}$

Figure 12: Spatio-temporal distribution of force coefficients at $\beta = 30°$

where S_{xy} denotes cross-spectral density of the quantity ($C_{x,n}$ or $C_{y,n}$) at two points separated by a distance Δz, and S_{xx}, S_{yy} are auto-spectral densities; angular brackets denote ensemble averaging, however ergodicity assumption is used to relate that to time averaging. The coherence plot of $C_{y,n}$ indicates that spanwise correlation is very high (over nearly the entire cylinder span) at the vortex shedding frequency, but is small at other frequencies, which is expected based on literature. $C_{x,n}$ however is not that highly correlated along the span even

19

at the peak vortex shedding frequency.

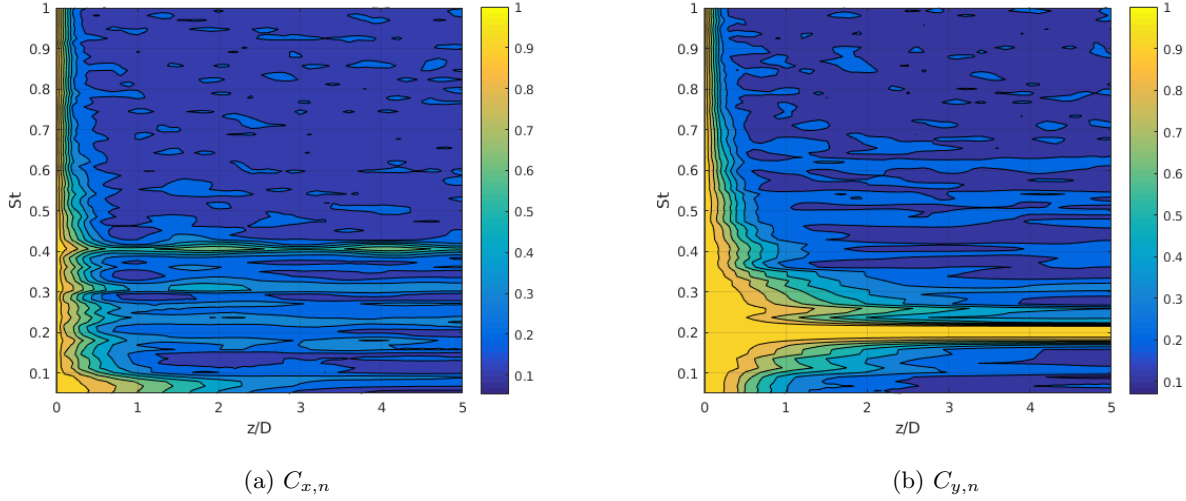(a) $C_{x,n}$ (b) $C_{y,n}$

Figure 13: Magnitude squared coherence, $\gamma^2(\Delta z)$ of transverse and longitudinal force coefficients, $C_{x,n}$ and $C_{y,n}$ for $\beta = 30°$ case.

5. Vortex-Induced Vibration Results

A schematic of the computational setup for vortex-induced vibration (VIV) simulations is presented in Figure 14. The setup is the same as for the static simulations except for an additional mass-spring-damper system that determines the motion of the cylinder. The cylinder is constrained to move only in the cross-stream (y) direction. The y-component of the integrated aerodynamic surface force on the cylinder drives the mass-spring-damper system given by Eq. 5. Simulations are performed for eight inflow reduced velocities and two values of yaw angle, β $(= 0°$ and $45°)$.

In the simulations the mass ratio $m^* = m/(\rho\mathcal{V}) = 2.6$, where m is the mass of the cylinder, $\mathcal{V} = \pi(D^2/4).S$ is the volume of the cylinder, S is the cylinder span, and ρ is the density of the fluid flowing over the cylinder. The mechanical damping ratio of the system $\zeta = c/c_c$ is 0.001 where, $c_c = 2\sqrt{k.m}$ is the critical damping, and the spring stiffness k is related to the natural frequency, f_N by $k = m(2\pi f_N)^2$. The non-dimensional parameters, m^*, ζ, and reduced velocity, are selected to match the measurements of Franzini et al. (2013). This measurement dataset is referred as Exp II in this paper. The reduced velocity

is varied in the experiments by changing the freestream flow speed, which changes Re_D. In the simulations, the reduced velocity is varied by changing the spring stiffness, and Re_D is held constant. In addition to Exp II, the simulation results are also compared to another dataset reported in Khalak and Williamson (1997), which is referred as Exp III here. The values of m^* (= 2.4) and ζ (= 0.0045) in Exp III are slightly different from Exp II and the simulations.
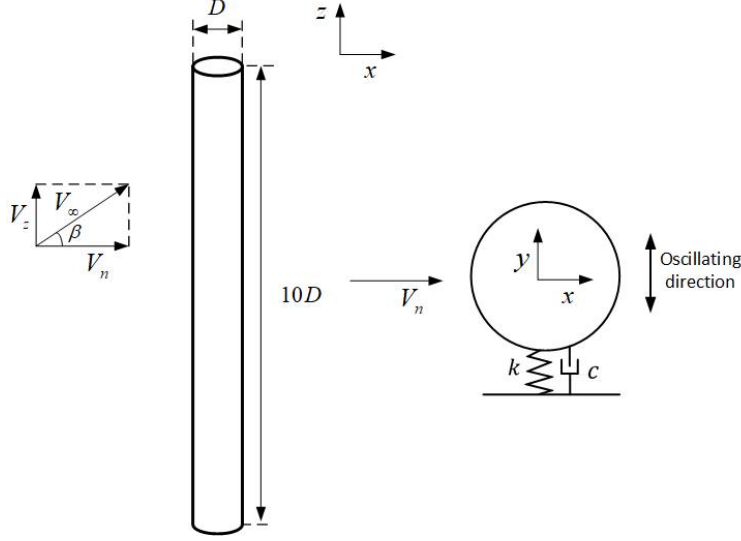

Figure 14: A schematic of the computational setup for oscillating cylinder simulations. The right figure shows a cross-sectional view. The inflow is set to an angle with respect to the cylinder axis, which is aligned with the z-axis of the coordinate system.

Figure 15 compares the predicted scaled mean displacement amplitude ($\bar{A}/D$) with the measurements of Exp II and III over a wide range of reduced velocity, $V_{R,n} = V_n/(f_N D)$, where f_N is the natural frequency of the system. The subscript n refers to the component of the velocity vector normal to the cylinder axis to accommodate yawed flow. Two different yaw angle flows are evaluated – $\beta = 0°$ and $45°$ – both at $Re_{D,n} = 20,000$.

Khalak and Williamson (1997) identified the following four distinct branches in the $\bar{A}/D$ versus $V_{R,n}$ plot of their VIV measurements for the zero-yaw case: the "initial excitation" branch, the "upper" branch, the "lower" branch, and the "desynchronization" branch. These are labeled and identified with solid black lines as best curve fits of the measured data in Fig. 15 (a). Note that the variation of $\bar{A}/D$ with $V_{R,n}$ is topologically different for systems with high m^*, e.g., measurements of Feng (1968) show two branches (multi-valued solution)

in the lock-in regime. For the selected low m^* system, $\bar{A}/D$ grows rapidly with $V_{R,n}$ in the *initial excitation* branch, reaches a peak in the *upper* branch, then reduces to 60% of the peak value in the *lower* branch, and finally drops to a negligible value at higher $V_{R,n}$ in the *desynchronization* branch. The current DES simulations agree very well with the data (particularly with Exp III) in the *initial excitation* and *upper* branches. The peak amplitude is well captured and occurs around $V_{R,n} = 4.76$, which corresponds to the peak vortex shedding Strouhal number, $St_p = 0.21$ for a stationary cylinder. The predicted amplitude is slightly lower than the measurements in the *lower* and *desynchronization* branches. Considering the relatively large differences in the two sets of measurements (Exp II and Exp III), which provides an estimate of uncertainity/repeatibility, the prediction accuracy of the simulations is very good.
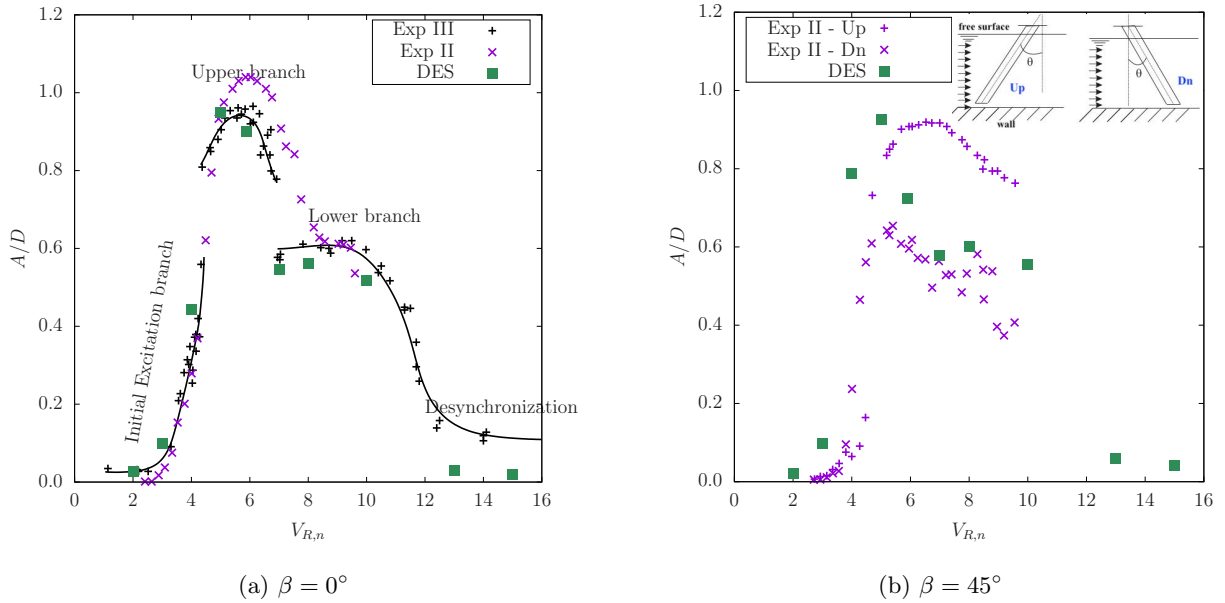

(a) $\beta = 0°$

(b) $\beta = 45°$

Figure 15: Comparison of predicted and measured non-dimensional mean amplitude, $\bar{A}/D$ over a range of reduced velocities $V_{R,n}$ for a) $\beta = 0°$, and b) $\beta = 45°$. The inset in the plot on the right shows the two setups (UP and DN) used in Exp II for yawed-flow measurements.

Figure 15 (b) compares the predicted VIV amplitude with the data from Exp II. The measurements were taken for two different configurations of the cylinder, which are shown in the inset in the figure. Since the top and bottom surfaces are not the same, the two configurations are not identical and the measured data for the two configurations shows a

large difference. Since the setup in the experiment is asymmetric (wall at the bottom and free surface on the top) and the fact that end plates were not used, end effects (finite-span effect) might be the reason for the observed differences between the two configurations. The predictions agree better with the "Up" configuration in the *initial excitation* and *upper* branches, and with the "Dn" configuration in the *lower* branch. Exp II did not collect any data at higher $V_{R,n}$ to test the prediction accuracy in the *desynchronization* branch.

5.1. Modes of Vortex Shedding

As seen in Figs. 15 and 17, the amplitude jumps up from the *initial excitation* branch to the *upper* branch, and jumps down from the *upper* branch to the *lower* branch as $V_{R,n}$ is increased. These jumps occur as the mode in which the vortex shedding occurs switches between two possible configurations. These modes are illustrated in Fig. 16 using schematics and iso-surface of the Q-criterion. In the '2S' mode, two single vortices shed alternately from either side of the cylinder in one cycle of cylinder motion, while in the '2P' mode, two pairs of vortices are shed from each side of the cylinder in one cycle. The 2P mode has been observed in the smoke visualizations of Brika and Laneville (1993). In the *initial excitation* branch, vortex shedding occurs in the 2S mode, while in the *lower* branch, it switches to the 2P mode. In the *upper* branch of the lock-in regime, the vortex shedding switches between the 2S and 2P modes. Other modes can also be observed (e.g., 2P+S and P+S modes) in forced vibration motion.

5.2. Independence Principle in VIV

This section investigates the validity of the *independence principle* on displacement amplitude and oscillating frequency of an elastically-mounted cylinder undergoing VIV. Prior experiments (e.g., Jain and Modarres-Sadeghi (2013) and Franzini et al. (2013)) have investigated IP for a circular cylinder. Zhao (2015) investigated IP using DNS at Reynolds numbers (Re_D=150 and 1,000). Much higher Re_D is considered here and the DES methodology used here can scale to significantly larger Re_D without a substantial increase in computation cost.

The data from Franzini et al. (2013) (Exp II) is plotted in Fig. 17 (a) and the DES predictions in Fig. 17 (b) for the two yaw angles evaluated ($\beta = 0°$ and $45°$). The DES predictions show little difference between $\beta = 0°$ and $45°$ except around $V_{R,n} = 4$ and 6,

23

(a) 2S mode; $V_{R,n} = 4$

(b) 2P mode; $V_{R,n} = 8$

(c) $\beta = 0°$; $V_{R,n} = 4$

(d) $\beta = 0°$; $V_{R,n} = 8$

(e) $\beta = 45°$; $V_{R,n} = 4$

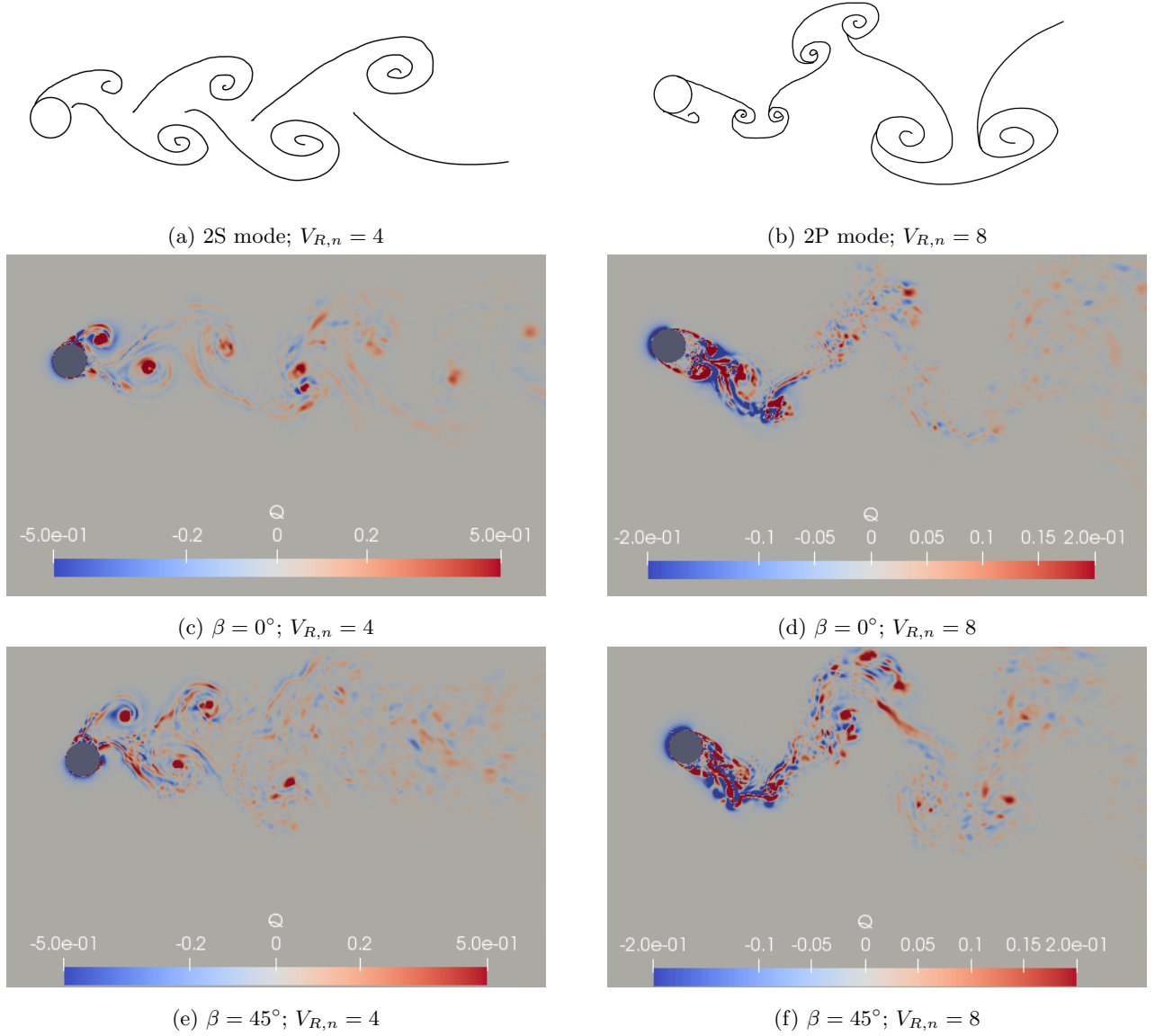(f) $\beta = 45°$; $V_{R,n} = 8$

Figure 16: Illustration of the two modes of vortex shedding observed in the simulations using schematics in (a) & (b), and iso-surfaces of the Q-criterion for $\beta = 0°$ in (c) & (d) and $\beta = 45°$ in (e) & (f).

where $\bar{A}/D$ is highly sensitive to changes in $V_{R,n}$. As far as the general variation of $\bar{A}/D$ with $V_{R,n}$ (identified by solid lines in Fig. 17 (b)) is considered, the predictions for both yaw angles show the same behavior, suggesting that the independence principle also holds for VIV. From the measurements however, one can only conclude that IP holds primarily in the Initial Excitation branch. The large difference in the measurements between the Up and Dn configurations for $\beta = 45°$ limits the verification of IP in VIV to the *initial excitation* branch.
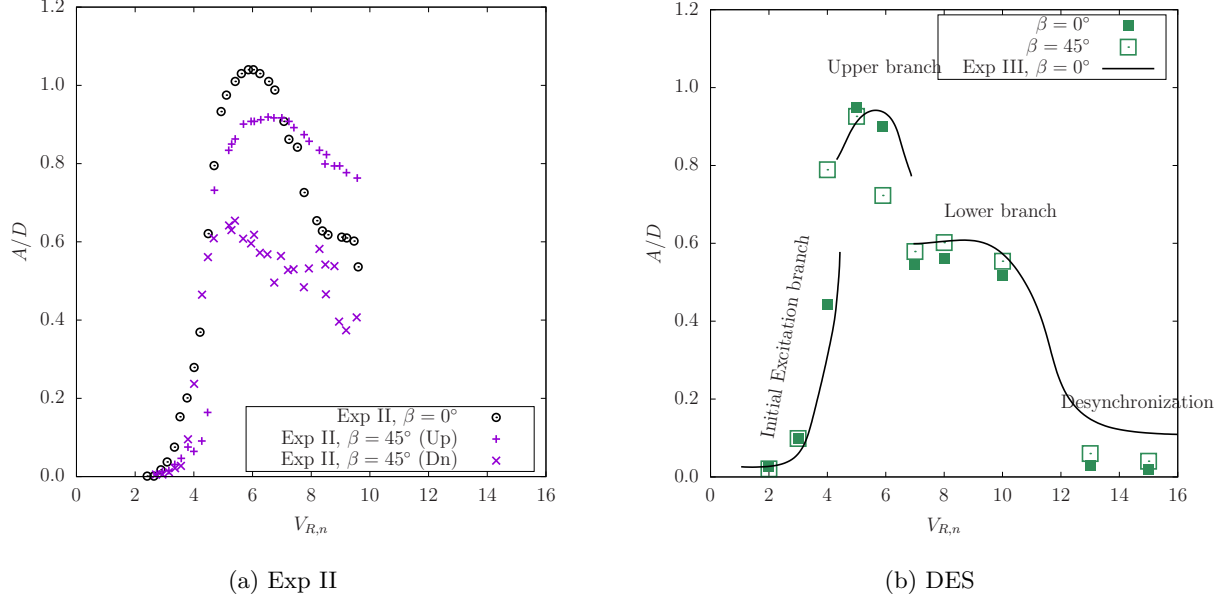
(a) Exp II   (b) DES

Figure 17: Scaled mean displacement amplitude $\bar{A}/D$ for $\beta = 0°$ and $45°$ degrees for a range of $V_{R,n}$ obtained from a) measurements from Exp II, and b) DES predictions with the data from Exp III for $\beta = 0°$ as a guide.

Figure 18 compares the normalized frequency (f/f_N) between the DES predictions and the measurements from Exp III over a range of $V_{R,n}$. The purple dashed line corresponds to the peak vortex-shedding frequency for a static cylinder $(St_p = 0.21)$ and the black dashed line corresponds to $f = f_N$. The simulations capture the variation of vortex-shedding frequency over the entire range of $V_{R,n}$ tested. In the *initial excitation* branch, the vortex shedding frequency (f), and hence f/f_N increases linearly with the reduced velocity $V_{R,n}$. Beyond resonance, which occurs around $f = f_N$, the vortex shedding frequency gets "locked-in" with the natural frequency of the system. This occurs in the *upper* and *lower* branches identified in Fig. 15 (a). The added mass of the fluid causes the lock-in frequency to be higher than f_N, particularly for low-m^* systems. As $V_{R,n}$ increases beyond lock-in, the vortex shedding frequency desynchronizes with the natural frequency and f/f_N again follows the purple line in the figure. Figure 18 also plots the simulation results for $\beta = 45°$, which are nearly coincident with the results for $\beta = 0°$, verifying IP.
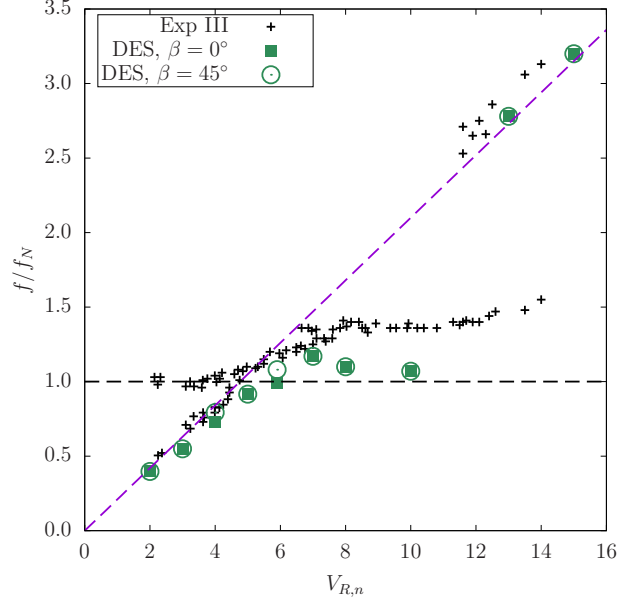
Figure 18: Non-dimensional frequency f/f_N for various reduced velocities $V_{R,n}$

6. Conclusion

A computational methodology based on a $k-\omega$ delayed detached eddy simulation (DDES) model is used to investigate aerodynamic loading on a smooth circular cylinder. Simulations are performed for the cylinder in normally-incident flow and yawed flow. The computational methodology is verified against experimental data in normally-incident flow ($\beta = 0°$) and yawed flow ($\beta = 30°$). The agreement between the simulations and the experiments for normally-incident flow is very good, and the results of the yawed flow simulations are in reasonable agreement with the measurements. These favorable comparisons demonstrate the ability of the DES methodology to accurately predict aerodynamic loading on static circular cylinders. Simulation results for different flow angles ($\beta = 0°, 15°, 30°,$ & $45°$) also verify the validity of the independence principle for β up to $45°$.

Simulations are also performed for an elastically-mounted rigid cylinder undergoing vortex-induced vibrations. The dynamics of the cylinder is modeled using a forced mass-spring-damper system with a low mass ratio and low damping, and the cylinder is constrained to move only in the transverse direction. The simulation results are compared with two sets of existing experimental data and the agreement of the predicted displacement amplitude and vortex shedding frequency with the measurements is found to be good over a wide range of

reduced velocity. The frequency lock-in phenomenon is captured by the simulations. Different modes of vortex shedding (2S and 2P) are observed in the simulations and are identified by plotting iso-surfaces of the Q-criterion. Results for two values of β (= 0° and 45°) are compared and, barring some difference in the regions where the displacement amplitude is highly sensitive to the reduced velocity, the independence principle is found to hold for circular cylinders in VIV up to a yaw angle of 45°.

7. Acknowledgments

References

Al-Jamal, H., Dalton, C., 2004. Vortex induced vibrations using large eddy simulation at a moderate reynolds number. Journal of fluids and structures 19 (1), 73–92.

Bearman, P. W., 1984. Vortex shedding from oscillating bluff bodies. Annual review of fluid mechanics 16 (1), 195–222.

Breuer, M., 1998. Large eddy simulation of the subcritical flow past a circular cylinder: numerical and modeling aspects. International Journal for Numerical Methods in Fluids 28 (9), 1281–1302.

Breuer, M., 2000. A challenging test case for large eddy simulation: high reynolds number circular cylinder flow. International Journal of Heat and Fluid Flow 21 (5), 648–654.

Brika, D., Laneville, A., 1993. Vortex-induced vibrations of a long flexible circular cylinder. Journal of Fluid Mechanics 250, 481–508.

Catalano, P., Wang, M., Iaccarino, G., Moin, P., 2003. Numerical simulation of the flow around a circular cylinder at high reynolds numbers. International Journal of Heat and Fluid Flow 24 (4), 463–469.

Davenport, A., 1995. The dynamics of cables in wind. In: Proceedings of Symposium on Cable Dynamics.

Dong, S., Karniadakis, G. E., 2005. Dns of flow past a stationary and oscillating cylinder at re= 10000. Journal of fluids and structures 20 (4), 519–531.

Evangelinos, C., Lucor, D., Karniadakis, G., 2000. Dns-derived force distribution on flexible cylinders subject to vortex-induced vibration. Journal of fluids and structures 14 (3), 429–440.

Feng, C., 1968. The measurement of vortex induced effects in flow past stationary and oscillating circular and d-section cylinders. Ph.D. thesis, University of British Columbia.

Franzini, G., Fujarra, A. L. C., Meneghini, J. R., Korkischko, I., Franciss, R., 2009. Experimental investigation of vortex-induced vibration on rigid, smooth and inclined cylinders. Journal of Fluids and Structures 25 (4), 742–750.

Franzini, G. R., Gonçalves, R. T., Meneghini, J. R., Fujarra, A. L. C., 2013. One and two degrees-of-freedom vortex-induced vibration experiments with yawed cylinders. Journal of fluids and structures 42, 401–420.

Guilmineau, E., Queutey, P., 2004. Numerical simulation of vortex-induced vibration of a circular cylinder with low mass-damping in a turbulent flow. Journal of fluids and structures 19 (4), 449–466.

Jain, A., Modarres-Sadeghi, Y., 2013. Vortex-induced vibrations of a flexibly-mounted inclined cylinder. Journal of Fluids and Structures 43, 28–40.

Khalak, A., Williamson, C., 1997. Fluid forces and dynamics of a hydroelastic structure with very low mass and damping. Journal of Fluids and Structures 11 (8), 973–982.

Kravchenko, A. G., Moin, P., 2000. Numerical studies of flow over a circular cylinder at re d= 3900. Physics of fluids 12 (2), 403–417.

Lucor, D., Foo, J., Karniadakis, G., 2005. Vortex mode selection of a rigid cylinder subject to viv at low mass-damping. Journal of Fluids and Structures 20 (4), 483–503.

Norberg, C., 2013. Pressure forces on a circular cylinder in cross flow. In: IUTAM Symposium on Bluff Body Wakes, Dynamics and Instabilities, eds H Eckelmann, JMR Graham, P Hierre, PA Monkewitz. pp. 275–278.

Pontaza, J. P., Menon, R. G., Chen, H.-C., 2009. Three-dimensional numerical simulations of flows past smooth and rough/bare and helically straked circular cylinders allowed to undergo two degree-of-freedom motions. Journal of Offshore Mechanics and Arctic Engineering 131 (2), 021301.

Sarpkaya, T., 2004. A critical review of the intrinsic nature of vortex-induced vibrations. Journal of fluids and structures 19 (4), 389–447.

Spalart, P., Jou, W., Strelets, M., Allmaras, S., et al., 1997. Comments on the feasibility of LES for wings, and on a hybrid RANS/LES approach. Advances in DNS/LES 1, 4–8.

Travin, A., Shur, M., Strelets, M., Spalart, P., 2000. Detached-eddy simulations past a circular cylinder. Flow, Turbulence and Combustion 63 (1-4), 293–313.

Williamson, C., Govardhan, R., 2004. Vortex-induced vibrations. Annu. Rev. Fluid Mech. 36, 413–455.

Xu, W.-H., Zeng, X.-H., Wu, Y.-X., 2008. High aspect ratio (l/d) riser viv prediction using wake oscillator model. Ocean Engineering 35 (17-18), 1769–1774.

Yeo, D., Jones, N., Meneveau, C., 2007. Characteristics of aerodynamic forces on a cylinder at different yaw and inclination angles under flow at high reynolds number. In: Proceedings of the 12th International Conference of Wind Engineering, Cairns, Australia. pp. 879–886.

Yeo, D., Jones, N. P., 2008. Investigation on 3-d characteristics of flow around a yawed and inclined circular cylinder. Journal of Wind Engineering and Industrial Aerodynamics 96 (10), 1947–1960.

Yeo, D., Jones, N. P., 2011. Computational study on aerodynamic mitigation of wind-induced, large-amplitude vibrations of stay cables with strakes. Journal of Wind Engineering and Industrial Aerodynamics 99 (4), 389–399.

Yeo, D., Jones, N. P., 2012. Aerodynamic forces induced by vertically oscillating incoming flow on a yawed horizontal circular cylinder. Journal of Wind Engineering and Industrial Aerodynamics 104, 188–195.

Yin, Z., Reddy, K., Durbin, P. A., 2015. On the dynamic computation of the model constant in delayed detached eddy simulation. Physics of Fluids 27 (2), 025105.

Zdravkovich, M. M., 2003. Flow around Circular Cylinders: Volume 2: Applications. Vol. 2. Oxford university press.

Zhao, M., 2015. The validity of the independence principle applied to the vortex-induced vibration of an inclined cylinder in steady flow. Applied Ocean Research 53, 155–160.

Zhao, M., Cheng, L., Zhou, T., 2009. Direct numerical simulation of three-dimensional flow past a yawed circular cylinder of infinite length. Journal of Fluids and Structures 25 (5), 831–847.